LASER & PHOTONICS REVIEWS
www.lpr-journal.org

Pixelation with Concentration-Encoded Effective Photons for Quantitative Molecular Optical Sectioning Microscopy

*Geng Wang, Rishyashring R. Iyer, Janet E. Sorrells, Edita Aksamitiene, Eric J. Chaney, Carlos A. Renteria, Jaena Park, Jindou Shi, Yi Sun, Stephen A. Boppart, and Haohua Tu**

Irreproducibility in molecular optical sectioning microscopy has hindered the transformation of acquired digital images from qualitative descriptions to quantitative data. Although numerous tools, metrics, and phantoms have been developed, accurate quantitative comparisons of data from different microscopy systems with diverse acquisition conditions remains a challenge. Here, they develop a simple tool based on an absolute measurement of bulk fluorophore solutions with related Poisson photon statistics, to overcome this obstacle is developed. Demonstrated in a prototypical multiphoton microscope, this tool unifies the unit of pixelated measurement to enable objective comparison of imaging performance across different modalities, microscopes, components/settings, and molecular targets. The application of this tool in live specimens identifies an attractive methodology for quantitative imaging, which rapidly acquires low signal-to-noise frames with either gentle illumination or low-concentration fluorescence labeling.

1. Introduction

With the call for public biological image archives, increasing awareness has been raised to improve the quantification[1] and reproducibility[2] of molecular (e.g., fluorescence) optical sectioning microscopy, including laser-scanning confocal/multiphoton microscopy and light-sheet microscopy. These aspects require rigorous quality control that can be loosely divided into 15 relatively independent subtasks/goals (Table S1, Supporting Information).[1–3] One systematic effort has performed 6 of these subtasks (Figure S1, Supporting Information) for wide-field and confocal laser-scanning microscopy platforms across imaging core facilities[3] but has not engaged the other 9 subtasks. More importantly, the corresponding tools, metrics, phantoms, and protocols would overburden a portable imaging facility, which requires one comprehensive calibration per travel to image often non-transportable living specimens. The lack of a simple quality-control tool has hindered the widespread application of portable label-free laser-scanning multiphoton microscopy in dermatology[4] and neurosurgery.[5]

Numerous designs of various live-cell imaging modalities[6] have challenged the development of a general quality-control tool. In this study, we propose a universal solution that engages all 15 subtasks with minimal calibration procedures, based on the simultaneous label-free auto-fluorescence multi-harmonic microscopy (SLAM) that integrates 4 modalities of two- and three-photon excited fluorescence and harmonics (2PF, SHG, 3PF, and THG).[7] We upgrade this system to a portable system[8,9] (pSLAM) and an extended version (eSLAM) that incorporates a stabilized (>2000 h) fiber supercontinuum source[10] (Figure S2, Supporting Information). The corresponding "label-free" aspect not only renders 2 sample-dependent subtasks irrelevant, but also mitigates plausible phototoxicity during time-lapse imaging[9] by inline monitoring the intrinsic phototoxicity indicator of elevated auto-fluorescence,[11] which has been linked to impaired cell cloning.[12] Also, the use of multiphoton illumination ensures negligible out-of-focus background, while the resulting simultaneous multicolor detection at single-band excitation ensures aberration-free chromatic co-registration.[7] In this way, only 10 subtasks remain relevant (Table S1, Supporting Information).

With the deterministic (coherent) spectral broadening in a single-mode fiber[9,10,13] that guarantees stable illumination via laser-microscope alignment decoupling[14] (**Figure 1**), we realize this elusive tool using diverse elements of photo-detection

G. Wang, R. R. Iyer, J. E. Sorrells, E. Aksamitiene, E. J. Chaney, C. A. Renteria, J. Park, J. Shi, Y. Sun, S. A. Boppart, H. Tu
Beckman Institute for Advanced Science and Technology
University of Illinois at Urbana-Champaign
Urbana, IL 61801, USA
E-mail: htu@illinois.edu

G. Wang, R. R. Iyer, J. Shi, Y. Sun, S. A. Boppart, H. Tu
Department of Electrical and Computer Engineering
University of Illinois at Urbana-Champaign
Urbana, IL 61801, USA

J. E. Sorrells, C. A. Renteria, J. Park, S. A. Boppart
Department of Bioengineering
University of Illinois at Urbana-Champaign
Urbana, IL 61801, USA

The ORCID identification number(s) for the author(s) of this article can be found under https://doi.org/10.1002/lpor.202400031

[The copyright line for this article was changed on 2 August 2024 after original online publication.]

DOI: 10.1002/lpor.202400031

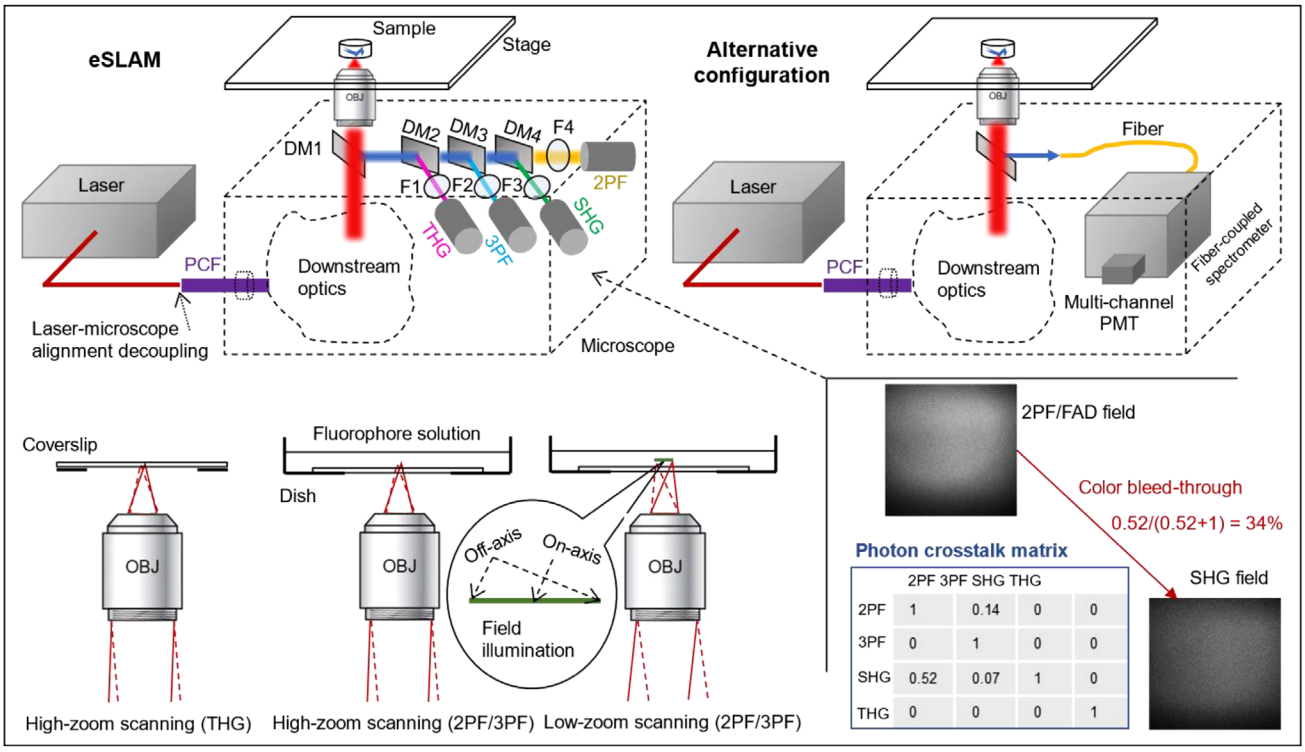

Figure 1. Schematic of eSLAM with built-in quality control. The inverted microscope (see Figure S2, Supporting Information for more details) consists of a source femtosecond laser, a spectrum-broadening module based on photonic crystal fiber (PCF), subsequent relaying optics with a mechanical stage to perform high/low-zoom 2PF/3PF "imaging" of a fluorophore solution at 15 ± 5 μm depth and THG imaging of coverslip interface (bottom left), and photo-detection paths with specific dichroic mirrors (DM) and optical filters (F) corresponding to 4 modalities (THG, 3PF/NADH, SHG, and 2PF/FAD), along with an alternative configuration with optical fiber-coupled spectral detection module (upper right). The optical alignment of the laser and the microscope is decoupled (i.e., laser-microscope alignment decoupling) because the misalignment of the former can be easily detected by the altered output spectrum of the PCF (see ref. [14] for details). Inset: measured bleed-trough from illumination field of 2PF/FAD to that of SHG and resulting photon crosstalk matrix for 4 modalities.

not directly related to imaging quality control[15–22] (Table S2, Supporting Information). Our tool, termed as Pixelating with Concentration-encoded Effective Photons (PCEP), integrates 3 independent subtasks to "image" fluorophore solutions with known concentrations,[23] while makes the other 7 subtasks dependent or feasible (Table S1, Supporting Information). This leads to a rather simple procedure to monitor hardware failure or degradation over time for fluorescence microscopy (including SLAM-based imaging), in contrast to a closely related approach that integrates 2 of the 3 independent subtasks.[24] Also, PCEP is validated by other forms/modalities of molecular optical sectioning microscopy with point-like (Table S3, Supporting Information) or camera-like photo-detection (see below), implying its broad applicability to alternative designs (Figure S3, Supporting Information). This may unify often proprietary image pixel representations from different microscopy vendors with a unit of absolute measurement (effective photon) directly related to the local concentration of a (labeled) molecule of interest.

2. Results

2.1. In Situ Absolute Measurement using Stable Illumination

Typically, the performance of a photodetector is either measured without placing it in situ (in a pre-aligned microscope with fixed optical components and alignments) or simply taken as original factory calibration without measuring over time, both of which are unsuitable for monitoring plausible failure or degradation over time. It is thus an important progress to measure a photomultiplier tube (PMT) in situ, using homogeneous samples such as the solutions of reduced nicotinamide adenine dinucleotide (NADH)[15] and flavin adenine dinucleotide (FAD), i.e., well-known intrinsic fluorophores in cellular metabolism. A similar experiment has allowed absolute measurement of multiphoton excitation molecular cross-section,[16] suggesting the feasibility to correlate (encode) the concentration of a fluorophore in solution with the number of detected photons. Motivated by these studies, we aimed to assess analog photo-detection performance by a simple in situ absolute measurement, using the illumination from a fiber supercontinuum laser with stable beam pointing, spatial mode propagation, and spectral power.[10]

Analog photo-detection noise consists of Poisson noise that includes the shot noise and excess noise[17] (i.e., multiplicative noise), and non-Poisson noise that includes the additive noise.[18] Thus, the Poisson-noise-dominated dynamic range (PDR) of a point-like analog photodetector can be determined experimentally wherever the non-Poisson noise is negligible. For detected fluorescence photons from a fluorophore solution within the PDR, the in situ measured signal-to-noise-ratio (SNR) in a small/flat-field area (e.g., several square micrometers[15]), i.e.,

mean versus standard deviation (STD) of the pixelated arbitrary intensity value from PMT analog output, satisfies the Poisson statistics of

$$\mathrm{SNR}|_{\mathrm{theory}} = \frac{m\bar{N}\ (\mathrm{signal})}{\sqrt{m\bar{N}}\ (\mathrm{noise})} = \sqrt{m\bar{N}} \text{ where } \bar{N} = \frac{\overline{N_D}}{1+\epsilon} \quad (1)$$

$$\mathrm{SNR}|_{\mathrm{experiment}} = \left.\frac{\mathrm{Mean}}{\mathrm{STD}}\right|_m = \sqrt{f_C C} \quad (2)$$

$$\mathrm{SNR}|_{\mathrm{experiment}} = \left.\frac{\mathrm{Mean}}{\mathrm{STD}}\right|_m = \sqrt{f_P P^n} \quad (3)$$

where $\overline{N_D}$ is the average signal/fluorescence photons detected by the PMT per pulse (or per excitation cycle to incorporate linear optical microscopy), ϵ is detector-dependent excess noise factor which is a constant for an analog PMT (20%–70%)[17] or zero for a photon-counting PMT (similar classification is applicable to array- or camera-like detectors), $\bar{N}$ is the corresponding effectively detected photons with a unit of "effective photon" at equal mean and STD, m is the number of pulses per pixel within one frame or over multiple frames[19] in one pixelated measurement, C is the concentration of a fluorophore of interest with a fitting parameter f_C to attain $m\bar{N}$ (Equation 1 and Equation 2), and n is the order of optical nonlinear process at average power P while f_P is the corresponding fitting parameter (Equation 1 and Equation 3).

Experimentally, we focused the illumination at a shallow depth (15 ± 5 μm) inside the solutions with a small field-of-view (FOV) of <10 × 10 μm^2, i.e., a high-zoom raster scanning through a microscope objective (Figure 1). By varying C of NADH solutions at a constant P or by varying P on a NADH/FAD solution with constant C, we tested these equations across three laser-scanning multiphoton microscopes operated at either one pulse per pixel[19] or hundreds of pulses per pixel (Table S3, Supplementary information), so that each experimental point of SNR involved ≥9000 pulses. The parameter f_C (or f_P) can be obtained from the single-parameter linear fit between experimental (mean/STD)^2 and C (or P^n) before signal saturation according to Equation 2 (or Equation 3), as shown in Figure S4 (or S5) (Supporting Information). Indeed, the theoretical log-scale linear relation between SNR and $\bar{N}$ (Equation 1) was validated by the corresponding experimental lines (Equation 2 or Equation 3) indicative of PDRs (**Figure 2**). This was valid despite the differences in microscope, n (2 or 3), m (1-320), variable/parameter (C/f_C or P^n/f_P), fluorophore (NADH or FAD), photodetector (regular or hybrid PMT), and the temporal window of signal collection optimized[9] for the largest PDR (Figure S6, Supporting Information). Without detecting any effect from somewhat variable imaging depth (Figure 1), we obtained the same effective photons from a given C at two PMT gains that produced 10-fold different arbitrary intensity values (Figure 2a, arrowheads). Thus, for fixed components and settings, the information of C was encoded by the effective photons from an absolute measurement, not the gain-dependent arbitrary intensity values.

These results suggest that Poisson noise-limited performance may be ensured over time by obtaining the same upper limit of a PDR at a certain gain (Figure 2a,c) and the same lower limit of the PDR at a high gain (Figure 2b,d). The PDR with variable P (Figure 2c, left) is often understood through the shot-noise-limited photon transfer curve (PTC) (Figure 2c, right), which has assessed PMTs using a LED source[19] and cameras using a uniform lump/LED illumination.[20] This offers an opportunity to evaluate the photon-number-resolving ability of a PMT. By THG "imaging" of a coverslip interface (homogeneous sample) in a manner like the high-zoom 2PF/3PF "imaging" of a fluorophore solution (Figure 1), we resolved >28 simultaneously arriving THG photons within a PDR upper limit of 28 effective photons (Figure 2c), even though the excess noise exceeded 0.5 photoelectron in the *continuous* histograms of PMT output[18] (Figure 2a, Inserts). Alternatively (and at a higher cost), *discrete* photon-number resolving ability has been demonstrated in a point-like superconducting transition-edge sensor[21] and a quanta image sensor[22] by lowering the readout noise of photo-detection below 0.5 photoelectron.

2.2. Multiphoton Illumination Fields Visualized in Bulk Solutions

Using the same eSLAM or pSLAM microscope, we switched from the above in situ absolute measurement to the visualization of illumination field[1] in fluorophore solutions, by simply switching the high-zoom scanning of <10 × 10 μm^2 to a low-zoom imaging across ≈250 × 250 μm^2 with a frame size of 1024 × 1024 pixels (Figure 1). Not surprisingly, the NADH solutions showed microscope-dependent but C-independent illumination fields pixelated with offset-removed arbitrary intensity values,[1] indicating the off-axis effects such as higher-order field curvature (**Figure 3**a,b) as opposed to on-axis illumination (Figure 1, bottom left). Within the same microscope (eSLAM), comparative results using NADH and FAD solutions also revealed the dependence of illumination field on n and modality/color/channel (Figure 3b,c). However, varying-P (varying-C) experiments using NADH solution(s) revealed no dependence of the illumination field on P or signal strength (C and imaging depth variation), indicating the reliability to visualize the illumination field in a bulk solution (Figure S7, Supporting Information). In fact, our custom-built microscopes had relied on the "flattening" of observed illumination field to optimize the alignment of relaying optics between laser source and photo-detection module.

The optimized 3PF/NADH field remained rather uneven due to high photon-order illumination, even though its predicted linear (one-photon) field was acceptably flat (Figure 3d). This unevenness might have limited the reported FOV (123 × 123 μm^2) of deep 3PF imaging.[25] Also, the comparison between the observed 2PF/FAD field with the predicted two-photon field of the observed 3PF/NADH field highlighted the noticeable dependence of the field illumination (Figure 3d, blue curves) on modality-specific detection path and efficiency[26] (Figure 1). This complexity from multi-color detection, along with the non-absolute measurement of the illumination fields (with sample-dependent PMT gains and other device settings of digitizer, amplifier, and/or attenuator), have complicated the isolated quantity control of flat-field illumination using fluorescent slides[27] and bulk solutions.[28]

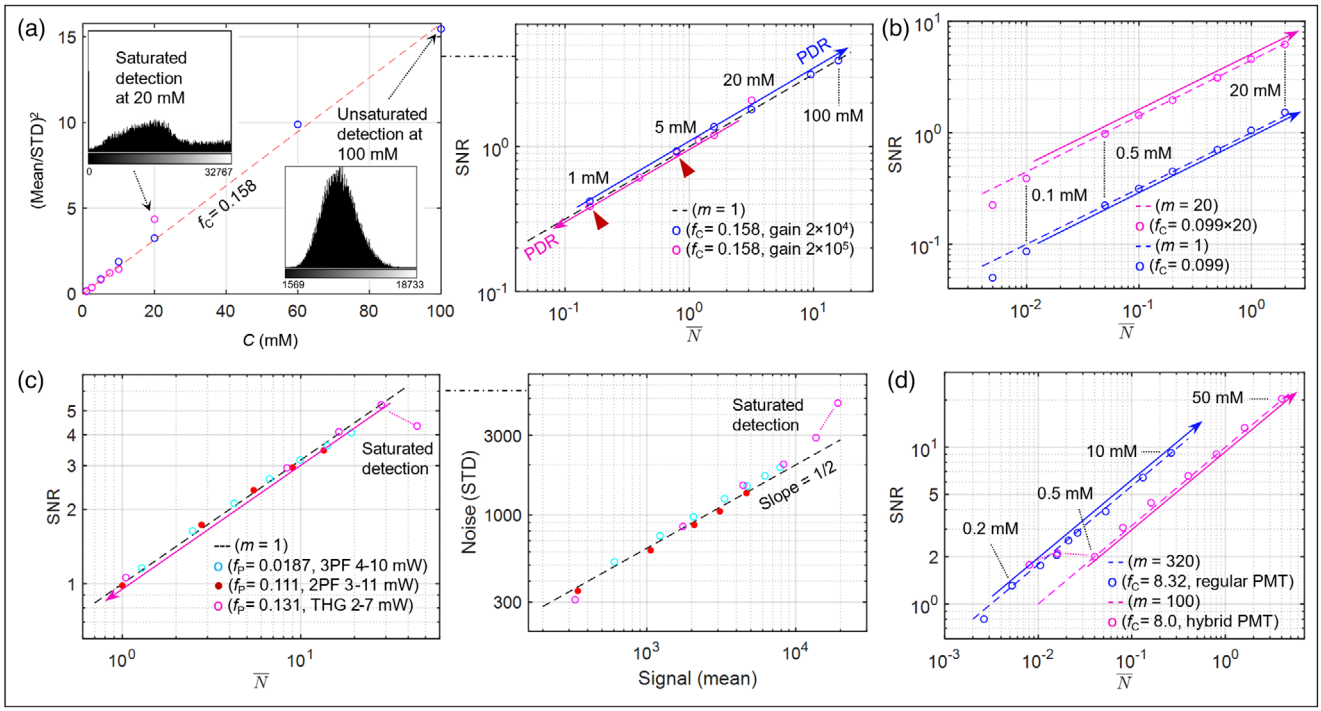

Figure 2. In situ absolute measurement of PDRs in three different multiphoton microscopes. a) Measurement of PDRs at two different PMT gains in pSLAM (colored circles and arrowed lines): parameter f_C obtained from a single-parameter linear fit (broken line) between experimental 3PF (mean/STD)^2 and C (NADH concentration) in two varying-C (P = 2.4 mW) experiments. Insets show unsaturated/saturated histograms at low/high gain. The right panel shows the corresponding log-scale PDRs from Equation 2 (colored circles and arrowed lines), where both PMT gains achieve 0.16 and 0.79 effective photons at 1 mM and 5 mM, respectively. The broken line indicates the prediction from Equation 1. b) Measurement of PDRs with different averaged frames in eSLAM (colored circles and arrowed lines): PDRs from varying-C (NADH) constant-P (16.8 mW) experiments (Equation 2) at PMT gain 4.8 × 10^5 corresponding to one frame and 20 frames along with prediction from Equation 1 (broken lines). c) Measurement of PDRs under different imaging modalities in pSLAM (colored circles/points and arrowed line): PDRs from varying-P experiments (Equation 3) at PMT gain 2 × 10^4 corresponding to 10 mM NADH/3PF, 10 mM FAD/2PF, and coverslip/THG along with prediction from Equation 1 (broken line); right panel shows their counterparts of photon transfer curves (PTCs). d) Measurement of PDRs with different type PMTs in traditional multiphoton microscopy (colored circles and arrowed lines): PDRs from varying-C (NADH) constant-P (15 mW for regular PMT, 30 mW for hybrid PMT) experiments (Equation 2) corresponding to a regular PMT (H7422P-40, Hamamatsu) at gain 1.1 × 10^6 and a hybrid PMT (R10467U-40, Hamamatsu) at gain 1.2 × 10^5 along with prediction from Equation 1 (broken lines).

2.3. Pixelating with Concentration-Encoded Effective Photons (PCEP)

Three key quality-control subtasks for reproducible and quantitative light microscopy are Poisson noise-limited detection, stable illumination, and flat-field illumination, which have been treated as independent goals[3] (Table S1, Supporting Information). After performing the three subtasks in two procedures detailed above, we attempted to integrate them into one simple procedure. Some previous attempts employed inhomogeneous samples and thus disengaged the flat-field illumination.[17,18] To engage this subtask, we quantitatively analyzed the pixelated arbitrary intensity values from the varying-C calibration (Figure 3b) and revealed the dependence of PDR on the size and location of region-of-interest (ROI) inside the FOV (Figure S8, Supporting Information).

We found an optimal size of 30 pixel × 30 pixel or 7.5 µm × 7.5 µm, termed as a super-pixel, which was small to ensure a uniform ROI (required for Equation 1) but large to generate a statistically convergent PDR (without noticeable deviation from the prediction) across the FOV (Figure 3b, right; Figure S8, Supporting Information). Because the f_c parameters associated with different super-pixels scale with locally averaged illumination field strengths, the information of one constant C is "encoded" as different effective photons for individual pixels (Figure 3b; Figure 3d *vs* Figure 3e) after converting the arbitrary intensity values to effective photons (Figures S4 and S5, middle panels, Supporting Information). In other words, the same effective photons at different pixels most likely represent different local C in a biospecimen, depending on their locations in the uneven illumination field. We thus term this representation "pixelation with concentration-encoded effective photons" (PCEP), which departs greatly from previous in situ measurements of homogeneous samples.[15,19]

Unexpectedly, the lower limit of the PDR associated with an on-axis super-pixel (~0.01 effective photon), i.e., detection limit due to the onset of specific non-Poisson noise that cannot be lowered by an increased m (Figure 2b), can be lowered by an increased off-axis extent down to ≈0.001 effective photon (Figure 3b, arrowheads). This effect suggests that the non-Poisson noise originates from local illumination field (which is worth future more detailed studies) rather than a constant additive noise[18] dictated by electronic settings such as the

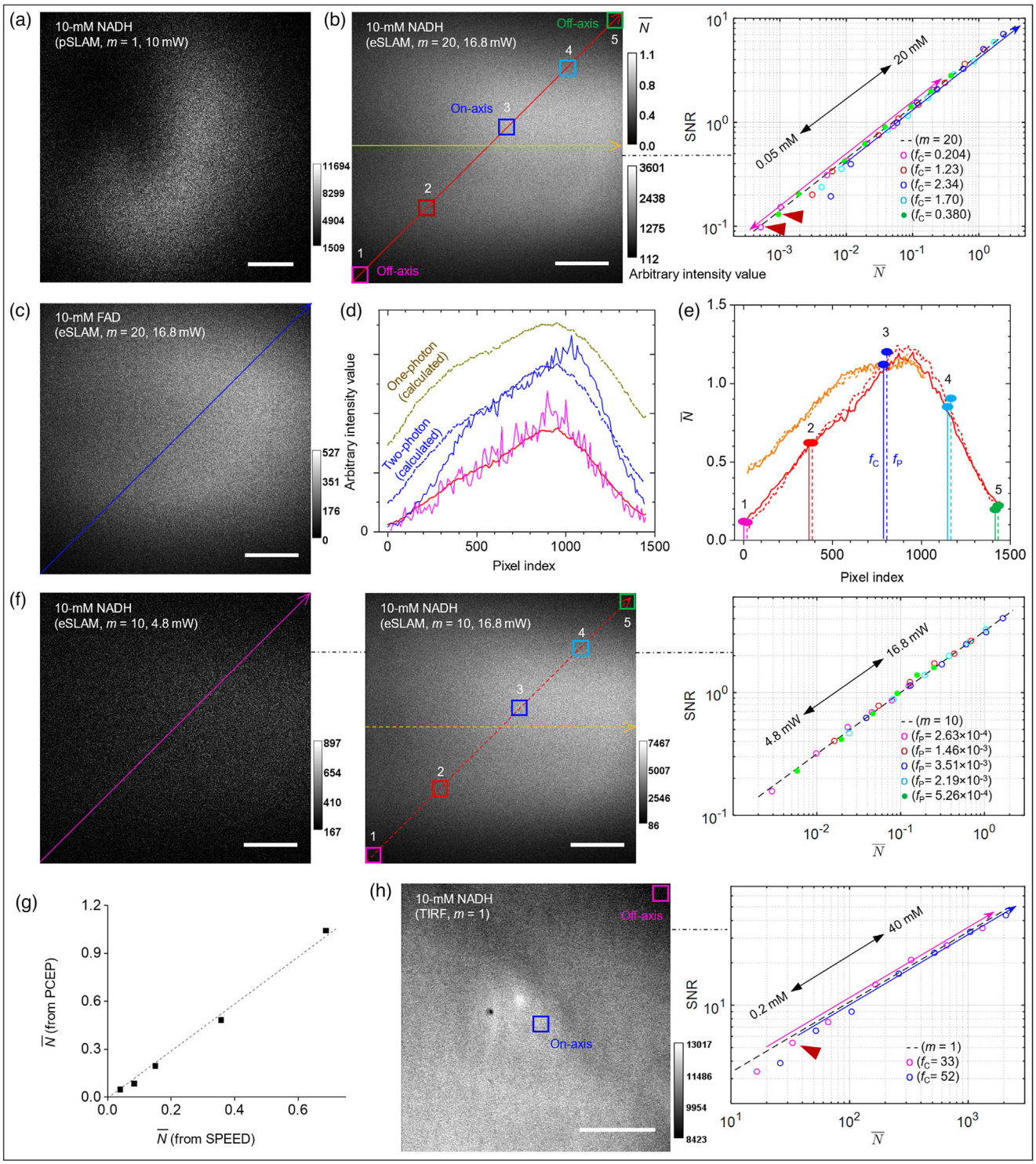

Figure 3. Characteristic features of PCEP. a) pSLAM illumination field (3PF) in NADH solution. b) eSLAM illumination field (3PF) visualized in NADH solution with predefined lines and super-pixels (boxes); right panel shows PDRs from varying-*C* (0.05/0.1/0.5/1/2/5/10/20 mM NADH) constant-*P* experiment (Equation 2) at PMT gain 4.8×10^5 corresponding to different super-pixels (colored circles/spots and arrowed lines) and prediction from Equation 1 (broken line). c) eSLAM illumination field (2PF) visualized in FAD solution. d) Diagonal line profiles in b, c, f-left with matched colors (solid lines) and calculated 1- or 2-photon counterpart of 3PF/NADH profile in b (broken lines). e) Diagonal/lateral line profiles in b-left and f-middle with matched colors/types consistent with properly scaled f_C/f_P parameters (vertical segments). f) eSLAM illumination field visualized in NADH solution using low *P* (left) or high *P* (middle); right panel shows SNR versus $\bar{N}$ relation from varying-*P* experiment (Equation 3) at PMT gain 4.8×10^5 corresponding to different super pixels (colored points) and prediction from Equation 1 (broken line). g) Comparison of effective photons in a vary-*C* NADH experiment obtained from either PCEP or single/multi-photon peak event detection (SPEED). h) TIRF illumination field (one-photon fluorescence) in NADH solution

temporal window (Figure S6, Supporting Information). Our PCEP produced an upper limit of ≈0.001 effective photon for the additive noise (the lower limit of PDR). The low illumination field strength (i.e., low signal) of off-axis super-pixels in comparison to on-axis super-pixels is countered by an enhanced photo-detection (absence of non-Poisson noise) to homogenize the detection dynamic range in C (≈0.1-20 mM NADH) across all super-pixels (Figure 3b, right), where the 0.05 mM data point in ROI 2/3/4 deviates from the prediction (broken line) due to the influence of Non-Poisson noise. The resulting detection limit of ≈0.1 mM NADH is termed as non-Poisson noise-equivalent concentration (NPNEC).

Thus, a misalignment-induced off-axis field illumination may produce a seemingly low detection limit in effective photons by the *in-situ* measurement of analog photo-detection, which would be mistakenly attributed to a high detection performance. This observation necessitates our integration of the three subtasks by PCEP. Also, the observed off-axis-enhanced photo-detection is especially beneficial for quantitative imaging of weak signals, using a strategy that rapidly acquires and averages single low SNR frames with either low-P illumination or low-C fluorescence labeling. This strategy mitigates the need to shrink the FOV[25] despite the highly uneven 3PF field illumination (Figure 3d). A similar strategy has been appreciated for reduced phototoxicity[29] but not for quantitative imaging.

2.4. Quality Control and Performance Benchmarking

From the perspective of routine quality control, a varying-P calibration (Figure 2c) is simpler than the varying-C calibration to perform PCEP, because it retains the absolute measurement of the latter using one constant C. After a varying-C calibration in eSLAM (Figure 3b) and 2 months of frequent biological imaging, we conducted one varying-P calibration that confirmed its equivalence to the varying-C calibration (Figure 3f), except for the absence of lower detection limit that required a more accurate power-meter. The f_P parameters associated with various super-pixels scaled with the corresponding f_C parameters, while the continuous illumination field in effective photons approximated its varying-C counterpart (Figure 3e). It is thus feasible to ensure reproducible 3PF/NADH imaging via the varying-P calibration at different time points, by first obtaining the same illumination field pixelated with effective photons and then the upper limit of additive noise from the weakest super-pixel. The former ensures no drift in optical alignment while the latter is necessary to monitor the degradation over time of a point-like photodetector without interference from field illumination.

To extend the single-color PCEP of 3PF/NADH to the multi-color/modality detection of eSLAM with different PMTs (Table S3, Supporting Information), we performed additional varying-P calibrations for 2PF/FAD, SHG, and THG imaging (Figure S5, Supporting Information). We thus established a photon crosstalk matrix to quantify the color bleed-through among 4 modalities regardless of PMT gain and other detection settings (Figure 1, see Methods). The flexibility in PMT gain allows tunable detection sensitivity and dynamic range (Figure S9, Supporting Information) for different biological samples or applications but would prevent an arbitrary intensity analogue of this crosstalk matrix for objective quantification. In fact, the photon crosstalk matrix had guided our selections of excitation bands, dichroic mirrors, and optical filters (Figure 1) in a feed-back process to minimize signal crosstalk while retaining detection efficiency.

We measured the point spread function (PSF) of eSLAM using ≈100-nm fluorescent beads and confirmed near diffraction-limited lateral-axial resolution (Figure S10, Supporting Information). Because any degradation of PSF will weaken the effective photon-pixelated illumination field, this PSF measurement becomes a dependent subtask that only requires one-time quality control effort, which can be guaranteed if no change is detected from routine PCEP calibrations. Thus, an automatic 3D microscope stage with repeatable positioning[3] (required for the PSF measurement) becomes an optional quality-control subtask, as it is neither needed in PCEP (using a manual 1D stage) nor in some applications free of multi-FOV stitching (e.g., cell culture-based drug testing and clinical imaging[4,5]). In this way, 6 major quality-control subtasks[3] can be reduced to one routine procedure (Figure S1, Supporting Information) especially beneficial for portable imaging.

To test the benchmarking by PCEP, we compared the C-encoded effective photons from PCEP and those from time-tagged computational photon-counting[23] in the experiment of Figure 2b. The two independent methods yielded consistent results except for a proportional factor of 1.46 (Figure 3g), which requires more detailed studies to understand. Overall, eSLAM attained an upgrade over SLAM to perform fluorescence lifetime imaging microscopy (FLIM) (Figure S11, Supporting Information). Using safe illumination powers that empirically avoided the phototoxicity of elevated auto-fluorescence,[9,11] we compared the performance of SLAM-based and conventional multiphoton microscopes in optical metabolic imaging of NADH and FAD.[30] We identified a surprising advantage of eSLAM, i.e., a higher NADH imaging sensitivity by 3PF over 2PF (Table S3, Supporting Information). It is this pixelwise ability to encode C that separates our study from a reported performance comparison among optical sectioning microscopes, which also converted the arbitrary intensity values of point- and camera-like detectors to effective photons.[31] To test the applicability of PCEP to camera-like detectors, we performed the varying-C NADH calibration on EMCCD camera of a total internal reflection fluorescence (TIRF) microscope (Figure S7, Supporting Information). The validity of PCEP was confirmed with an NPNEC of ≈0.5 mM under the assumed safe illumination (Figure 3h, arrowhead).

2.5. Biological Demonstration via eSLAM Imaging

To demonstrate the quantification by PCEP, we conducted eSLAM imaging on unlabeled cells and extracellular components of an *ex vivo* rabbit kidney (**Figure 4a**). We converted arbitrary intensity values to effective photon counts using the PCEP method and, as a first approximation, ignored the differences in illumina-

at 405-nm excitation with on-axis and off-axis super-pixels (exposure 0.1 ms); right panel shows PDRs from varying-C (NADH) constant-P experiment (Equation 2) corresponding to the two super-pixels (colored points and solid lines) and prediction from Equation 1 (broken line). Scale bars: 50 µm.

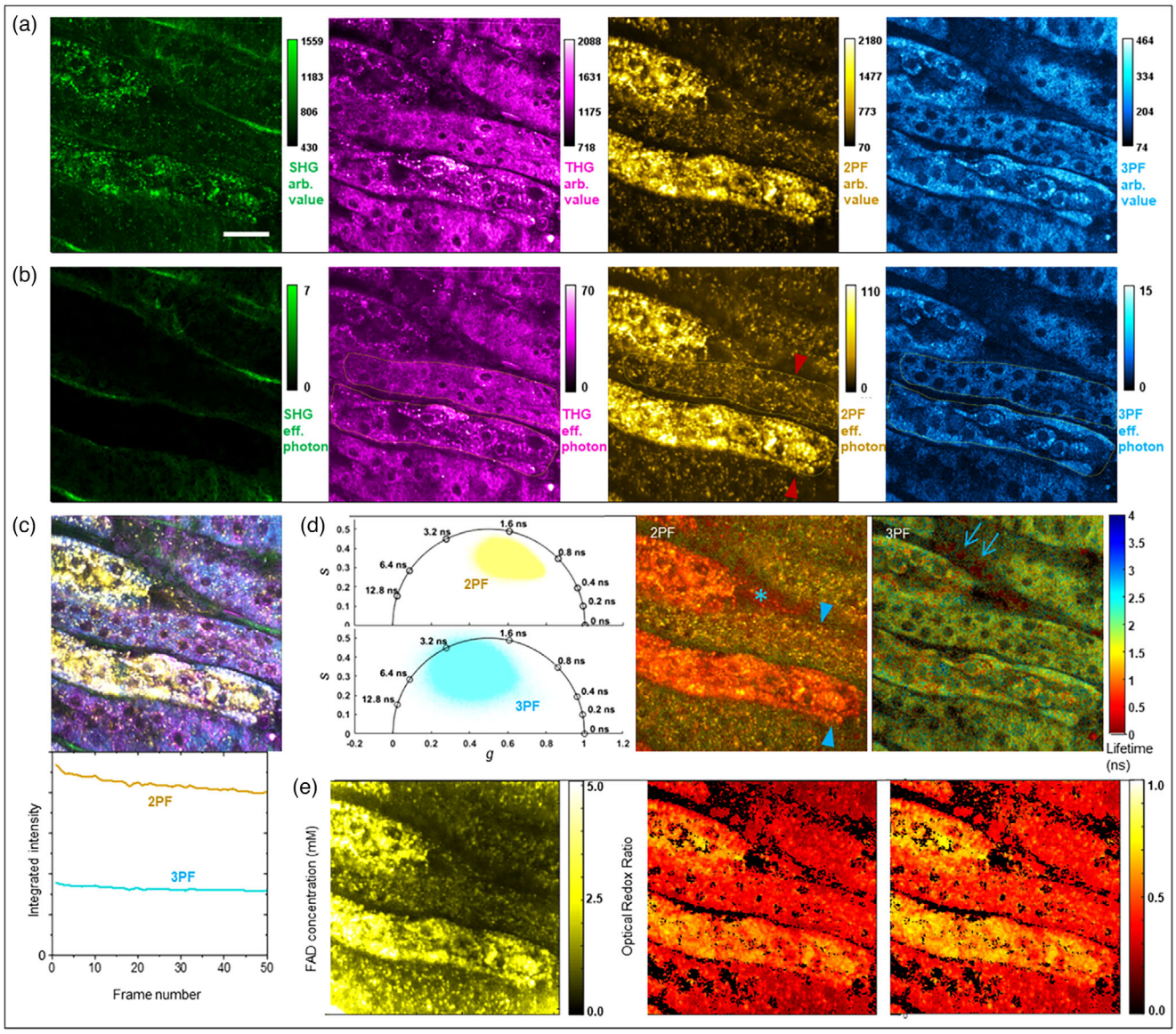

Figure 4. Quantitative biological imaging by eSLAM. Scale bar: 50 µm. a) Arbitrary intensity value-pixelated images of *ex vivo* rabbit kidney at ≈15 µm imaging depth with SHG, THG, 2PF/FAD, and 3PF/NADH signals (50-frame summation). b) Corresponding effective photon-pixelated images after color bleed-through correction showing kidney epithelial cells with average effective photons per pixel of 27 (THG), 30 (FAD), and 3 (NADH). c) Composite image (top) and real-time monitoring of FAD/NADH photo-bleaching during time-lapse imaging (bottom). d) phase plots (left) and corresponding FLIM images of FAD and NADH (right) showing fluorescence lifetime with intensity overlay (9-pixel averaging over neighboring pixels); arrowheads: kidney tubules, asterisk: FLIM data has better discrimination in distinguishing the two kidney tubules compared to the intensity in b) arrows: hemoglobin Soret fluorescence. e) Image of FAD concentration corrected for uneven field illumination (left) and related images of optical redox ratio with (middle) and without the field correction (right).

tion fields for different modalities (Figure 3d, blue curves). Then, based on the calibrated photon crosstalk matrix in Figure 1, we corrected color bleed-through across modalities and quantified the kidney cells across the channels of 2PF/FAD, 3PF/NADH, and THG (Figure 4b). The weak SHG signal from basement membrane-like collagen, which would otherwise be obscured by a strong 2PF bleed-through, became clearly discernible (compare Figure 4a,b, green contrast). Importantly, gradual photo-bleaching occurred in 2PF and 3PF (full FOV) without the phototoxicity of elevated auto-fluorescence[11] during time-lapse imaging (Figure 4c). The frame acquisition time (≈0.33 s) of eSLAM using a resonant-galvanometer scanner allowed real-time monitoring of photo-bleaching and phototoxicity, in contrast to SLAM with a slow galvanometer-galvanometer scanner.

We produced the corresponding FLIM images and phasor plots for 2PF/FAD and 3PF/NADH signals (Figure 4d). Interestingly, two different kidney tubules distinguishable by 2PF intensity and lifetime can be attributed to the proximal and distal tubules[32] with presumably different cellular metabolism (Figure 4b,d, arrowheads). The FLIM data not only distinguishes

the two tubules better than 2PF intensity (Figure 4d, star), but also uniquely identifies the hemoglobin Soret fluorescence (peaked at 438 nm) from blood cells by its ultrashort lifetime[33] (Figure 4d, arrows). Local absolute concentrations of FAD (or NADH) can be derived from the phasor plots[34] (Note S1, Supporting Information) and corrected for the uneven 2PF/3PF field (Figure 4e, left). The corresponding image of optical redox ratio $C_{FAD}/(C_{NADH}+C_{FAD})$ is thus obtained with rather small dependence on the field correction (Figure 4e, right panels). Further refinement of this metabolic imaging is needed to discriminate NADH against NADPH (or FAD against cellular lipofuscin) in the 3PF (or 2PF) modality.[30]

To reveal the enabling role of PCEP in microscopy-biology interaction, we tested eSLAM in numerous cell/tissue specimens and validated the safe illumination power (Table S3, Supporting Information) while confirmed no saturation (Figure 2a, Insets) under a moderate PMT gain. We obtained the largest biological signal from mouse skull (THG up to 11 effective photons per pulse), which would saturate the photon-counting in SLAM under the same excitation (Figure S12, Supporting Information). Also, the generally low cellular NADH signal in comparison to cellular FAD signal favors 1110 nm (eSLAM) over 1030 nm (pSLAM) for excitation (Table S3, Supporting Information). This performance benching creates the need to build a portable eSLAM microscope. Moreover, the observed dependence of illumination field on free-space detection path/modality (Figure 3d, blue curves) points to an attractive alternative of optical fiber-coupled 16-channel spectral detection module[35] free of this dependence (Figure 1, upper right), which would also permit tunable excitation.[14] In this prototypical process to optimize nonlinear optical imaging, PCEP allowed a custom-built microscope to co-evolve with the biology of interest toward reproducible, quantitative, gentle, and portable imaging.

3. Discussion

The quality-control tool of PCEP is generally applicable to molecular optical sectioning microscopy with a well-defined planar illumination field. With PCEP, image processing can be limited to rather simple tasks such as shading correction[26] (Figure S13, Supporting Information), without any deconvolution or reconstruction that may prevent real-time visualization and/or quantitative analysis. Although we have only demonstrated PCEP in laser-scanning multiphoton microscopy and wide-field TIRF microscopy, the underlining mechanism may be broadly applicable to confocal microscopy and light-sheet microscopy.[28] This is timely due to the recent standardization of laser-scanning confocal microscopy. PCEP requires only a bulk fluorophore solution as standard sample, and thus avoids the special preparation of thin (≈200 nm) and flat uniform fluorescent samples.[26] After placing the illumination field inside the solution just like how biological imaging is done, the varying-*P* PCEP calibration becomes a simple procedure widely supported by commercial microscopes. The procedure may be automated for routine self-diagnostic quality control of a core (static) imaging facility. This automation will be particularly beneficial for a portable imaging facility because the embedded absolute measurement allows sensitive detection of any changes to laser source, photo-detection module, and relaying microscope optics.

Routine PCEP calibrations enable image pixel representation by the effective photons within a measured PDR (rather than an arbitrary intensity value). The error at each pixel is thus the squared root of the effective photons. This not only enables objective assessment of image quality but also supports a standard image format (Table S1, Supporting Information). Storing images in a standardized format permits quantitative comparison of images from not only the same microscope over time, but also diverse microscopes with rich sample types, molecular targets, and imaging contrasts (e.g., fluorescence, harmonics,[7] and molecular vibration[14]), allowing buildup of image archives for large-scale reanalysis. Also, PCEP may empower photon-counting detection[7,18,19] to measure PDR and encode *C*, so that a specific imaging experiment can be reproduced by obtaining the same effective photon-pixelated image regardless of photodetection mode. The resulting *C*-encoded effective photons may be correlated with the local concentration of an intrinsic[34] or fluorescence-labeled biomolecule of interest.[1] Beyond single-color imaging, proper PCEP calibration can quantitatively correct the color bleed-through in multicolor imaging of multiple biomolecules. Finally, by taking account of phototoxicity, PCEP can benchmark the performance of different modalities or microscopes to image the same molecular targets.

Beyond the quality control of a preexisting microscope, PCEP can serve as a precision measurement tool to optimize a custom-built microscope, with a detection limit down to 0.001 effective photon and a dynamic range of more than 3 orders of magnitude for a typical PMT at one gain (Figure S14, Supporting Information). Our PCEP-assisted upgrade of SLAM (photon-counting) to eSLAM (analog photo-detection) transforms a low signal rate of less than one effective photon per pulse to a high signal rate of up to 11 simultaneously arrived effective photons per pulse under safe biological illumination. The "idealized" design of eSLAM may serve as the starting point to generalize PCEP to diverse designs of molecular optical sectioning microscopy. In this process, PCEP may play a similar enabling role by connecting microscopy design elements with interacting biological elements, such as fluorophore concentration, photobleaching/phototoxicity, targeted or labeled biomolecules, samples of interest, intended spatial/temporal resolution, etc. This connection will enable the optimization of microscope design elements such as the choice of imaging modality, illumination and photo-detection parameters, microscope objective, frame size and rate, etc. At large imaging depths, PCEP-calibrated quantification becomes susceptible to the interference of out-of-focus background in deep imaging,[25] which depends on sample absorption-scattering properties and thus requires specific protocol to estimate.[31] One way to navigate this challenge is to work with thin sectioned samples[36] and thin homogeneous fluorescent phantoms,[26] so that PCEP-based quality control may be extended to the wide-field epi-fluorescence microscopy with non-laser light sources.

4. Experimental Section

Optical Setup of eSLAM: Details of the laser source had been reported elsewhere.[10] The 5 MHz supercontinuum pulses from this source were sent into a 128-pixel 4f pulse shaper (femtoJock Box, BioPhotonic Solutions Inc.) to select an excitation band of 1110 ± 30 nm. The spectrally se-

lected pulses were then raster scanned by a resonant mirror (10 × 10 mm, 1592 Hz line rate, EOCP) and a galvanometer mirror (GVS011, Thorlabs), and finally focused by a microscope objective (UAPON 40XW340, N.A. = 1.15, Olympus) with up to ≈35 mW average power on the sample. A pair of identical achromatic doublets (AC254-050-C-ML – f = 50 mm, Thorlabs) and another pair of different achromatic doublets (AC254-030-C-ML – f = 30 mm, AC508-100-C-ML – f = 100 mm, Thorlabs) were used for 4f telecentric resonant-galvanometer beam steering, while the latter also expanded the beam to fill the back focal pupil plane of the objective (Ø10.35 mm). The actual/safe power on the sample was adjusted by a neutral density (ND) filter while the corresponding pulse width was compressed to near-transform-limited value (≈60 fs, FWHM) by the pulse shaper.[14] Average incident power at the sample plane was measured by a microscope slide power meter (S175C, Thorlabs). The photo-detection of eSLAM followed that of SLAM except for the replacement of photon-counting PMTs with analog PMTs (Table S3, Supporting Information). The whole system functioned as an inverted multiphoton microscope.

Signal Acquisition and Processing (General): The pulse repetition rate of the laser source (40 MHz) was divided to 10 MHz by a frequency divider (PRL-260BNT, Pulse Research Lab) and distributed by a fanout line driver (PRL-414B, Pulse Research Lab), and then used as the master clock to synchronize the resonant mirror and subsequent signal acquisition. For the resonant mirror, the active acquisition length was designed to occupy the central 65% of the sinusoidal line profile (spatial fill fraction), with one pulse per pixel per frame (i.e., pixel dwell time 0.2 µs). The PMT-detected 2PF and 3PF signals were first sent to high-speed current-to-voltage conversion amplifier unit (C5594-12, Hamamatsu) with 1.5 GHz cutoff frequency. The converted voltage signals were then digitized by a 2 GHz dual-channel high-speed digitizer (ATS9373, AlazarTech). For high dynamic range calibration of photo-detection using a NADH/FAD solution, a 20 dB attenuator was connected after the amplifier to match the range of digitizer input voltage (± 400 mV). The signals from SHG and THG modalities were amplified by a 60 MHz bandwidth amplifier (TIA60, Thorlabs) and digitized by a 125 MS s^{-1} digitizer (ATS9440, AlazarTech).

A GPU (GeForce RTX 2080, NVIDIA) enabled real-time image display and accelerated raw data process. This design supported a maximal frame (1024 pixel × 1024 pixel) rate of 3 Hz by bidirectional resonant scanning but was limited to ≈1.7 Hz by the storage of rapidly digitized 2PF and 3PF modalities. At 5 MHz repetition rate and 2 GS s^{-1} sampling rate, there are 400 sampling points between pulses. Because the fluorescence lifetime of FAD or NADH is less than 10 ns (20 sampling points), at least 95% of the data points are noise points. To avoid these noise points, the position of the maximum value within each line of fast scan was first found by superimposing the raw data of all the pixels in the line. Then, the custom data points near the maximum value position (time-gated window) were extracted using a custom LabVIEW-based GUI with 40 data points per pulse, 9 before the maximum value and 30 after the maximum value (Figure S15, Supporting Information). By implementing this algorithm in the GPU, most noise points were removed before storage.

Before performing PCEP, the offset values must be removed from all pixels of field illumination images.[1] For the vary-C (varying-P) experiment, the offset values are obtained from a field illumination image of blank control solution of $C = 0$ (or a fluorophore solution at $P = 0$). Then, parameter f_C (or f_P) is determined by the single-parameter linear fit between experimental $(\text{Mean}/\text{STD})^2$ from a small FOV or a ROI (or super-pixel) of field illumination images and C (or P^n). This produces an experimental SNR versus $\bar{N}$ relation (Equation 2 or Equation 3) to compare with the theoretical relation with known m (Equation 1), resulting in a measured PDR often with a distinguishable lower end that exhibits disagreement.

Signal Acquisition and Processing (FLIM): To validate the FLIM capability of eSLAM, the lifetimes of SHG (≈0.0 ns), NADH in 1 M HEPES (≈0.4 ns), Rhodamine B in water (≈1.7 ns), and Fluorescein in ethanol (≈3.4 ns) were tested using computational photon counting by employing the single- and multi-photon peak event detection (SPEED) algorithm.[23] Specifically, Rhodamine B and Fluorescein were used to calibrate the 2PF modality, NADH was used to calibrate the 3PF modality, and the temporal impulse response function (IRF) of the system was determined by SHG imaging of a urea crystal (Figure S11, top, Supporting Information). The estimated fluorescence lifetimes approximated the known values (Figure S11, bottom, Supporting Information). However, low fluorescence lifetimes (such as NADH and SHG) were biased slightly higher due to the limited bandwidth of collection electronics, and longer fluorescence lifetimes (Rhodamine B and Fluorescein) were biased to lower values, likely due to the low probability of collecting and properly time-tagging later-arriving photons when using one laser pulse per pixel and inferring the laser pulse synchronization.[23] The IRF of photo-detection had a full-width-half-maximum (FWHM) of 0.56 ns, slightly higher than previously reported IRFs estimated using SPEED which used a different PMT and faster digitization rates (0.32 ns IRF with 3.2 GS s^{-1} ADC or 0.23 ns IRF with 5 GS s^{-1} ADC). Despite these biases, existing eSLAM sufficiently revealed relative changes in fluorescence lifetime over the range of interest for NADH and FAD (Figure 4d).

Both SPEED and PCEP were used to quantify the average number of photons per pulse using different concentrations of NADH from 0.5 to 20 mM. Data was analyzed to determine the average number of photons per pulse per 1 mM NADH, resulting in 0.060 photons/pulse/1 mM NADH for SPEED and 0.068 photons/pulse/1 mM NADH for PCEP with a strong linear correlation ($R^2 = 0.998$, Figure 3g). A small percentage (<10%) of photon counts were being missed at the higher photon rates of the experimental data using SPEED, leading to values that are biased slightly lower due to the finite dead time of the system[23] (≈1.0 ns, or twice the sampling rate). The SPEED method requires high sampling rate (>1 GS s^{-1} with high consumption on acquisition and computation) to restore the original signal and time tag detected photons for FLIM imaging, whereas PCEP simply uses the integrated/averaged signal collected at lower digitization rates and supports up to 28 effective photons per pulse (Figure 2c) but does not time-tag the detected photons. The presented eSLAM system was capable of both SPEED and PCEP for quantification due to its versatile design.

Photon Crosstalk Matrix: The varying-P experiments for 4 different modalities (2PF, 3PF, SHG, and THG) not only calibrated the relation between pixel arbitrary intensity values and effective photons within individual modalities (Figure S5, Supporting Information), but also produced the color bleed-through across these modalities due to the simultaneous signal acquisition by eSLAM. The input signal of a given modality and related bleed-through to other modalities (columned percentages in Figure 1, Inset) were qualified using the converted effective photons from the arbitrary intensity values (Figure S5, middle panels, Supporting Information) over the full field-of-view of illumination (Figure 1, images). This removed any dependence of the resulting crosstalk matrix (Figure 1, Inset) on illumination power, PMT gain, or other device settings (which would be present if the arbitrary intensity value were used). Although the calibration was performed at specific PMT gains, the arbitrary intensity values at different gains could be calculated by the ratio of actual versus calibrated gain to produce a look-up table of arbitrary-intensity-value -to-effective-photon conversion. Despite this complexity, the photon crosstalk matrix remains constant for different PMT gains (as demonstrated in Figure 2a). It could be varied by changing the optical filters and dichroic mirrors of photo-detection module to minimize signal crosstalk (Figure 1).

The photon crosstalk matrix in Figure 1 was then divided by the total applied load in each modality to obtain the transfer function K:

$$K = \begin{vmatrix} 0.657 & 0.112 & 0 & 0 \\ 0 & 0.828 & 0 & 0 \\ 0.343 & 0.060 & 1 & 0 \\ 0 & 0 & 0 & 1 \end{vmatrix} \tag{4}$$

and the inverse matrix K^{-1}:

$$K^{-1} = \begin{vmatrix} 1.523 & -0.206 & 0 & 0 \\ 0 & 1.207 & 0 & 0 \\ -0.523 & -0.0012 & 1 & 0 \\ 0 & 0 & 0 & 1 \end{vmatrix} \tag{5}$$

Applying K^{-1} to each pixel of eSLAM images (Figure 4a) after arbitrary-intensity-value-to-effective-photon conversion resulted in the crosstalk-compensated images without field correction (Figure 4b).

Overview of Calibration and Data Processing in eSLAM: Software components of eSLAM had been discussed individually. With PCEP-based calibration that determine various data processing parameters, the digitized analog outputs of PMTs from a biological sample can be ultimately converted to effective photon-pixelated multimodal eSLAM images, and related fluorescence lifetime images and concentration images of targeted fluorophores (Figure S16, Supporting Information). Thus, eSLAM can serve as a starting point of quantitative imaging for diverse designs of molecular optical sectioning microscopy (Figure S3, Supporting Information).

Other Microscopes and Stage Focusing: Details of the SLAM microscope, pSLAM microscope, and traditional multiphoton microscope (MPM) had been reported in one paper,[7] a preprint[9] and two recent reports,[23] respectively. The main independent parameters of these laser-scanning microscopes were compared with those of eSLAM (Table S3, Supporting Information). The wide-field inverted TIRF microscope built upon a Zeiss Axiovert 200 M microscope was equipped with an oil immersion microscope objective (63x, NA 1.4) and a cooled Photometrics 512 Evolve EMCCD camera to image the fluorescence of single molecules or a thin (<200 nm typically) specimen.

The stage focusing of these microscopes was required for PCEP to visualize the illumination field in a bulk fluorophore solution inside a 35-mm glass (coverslip) bottom dish (Figure 1). For all laser-scanning inverted microscopes (eSLAM, pSLAM, and MPM), the interface between coverslip and the solution was detected by continuous low-zoom fluorescence imaging while manually positioning a microscope stage. Then, the illumination plane was placed ≈10 µm inside the solution using the stage. For the TIRF microscope, this interface was first marked with fiducial lines by a diamond knife and detected by the built-in bright-field imaging of the same microscope. The bright-field imaging was then switched to TIRF imaging while the corresponding illumination field was placed ≈10 µm inside the solution manually using the built-in stage of the microscope.

Preparation of Bulk Solutions: NADH (Grade I, Sigma) and FAD (94% dry wt., ThermoFisher Scientific) were dissolved in a 1 M HEPES buffer to maintain a stable pH. Rhodamine B and acridine orange were dissolved in sterile water. Fluorescein was dissolved in 100% ethanol.

Cell Culture: Human breast cancer cells MCF7 (ATCC HTB-22) were maintained in EMEM supplemented 10% FBS, 5 µg mL^{-1} insulin and 1% penicillin streptomycin antibiotic, and grown in an incubator at 37 °C with 5% CO_2. One day prior to imaging, cells were plated on poly-D-lysine coated 35 mm diameter glass-bottom imaging dishes (P35GC-0-10-C, MatTek) and incubated overnight in 2 mL of media to adhere.

Animal Tissue: All animal procedures were conducted in accordance with protocols approved by the Illinois Institutional Animal Care and Use Committee at the University of Illinois at Urbana-Champaign. The internal organs were obtained from ≈3-month-old 2.8 kg laboratory female New Zealand white albino rabbits (Oryctolagus cuniculus) (Charles River Laboratories, Wilmington, MA) bearing subcutaneous rabbit mammary tumors within 10 minutes post-mortem. The excised kidneys (or hearts) were immediately submerged in sterile Ca^{2+}/Mg^{2+}-free 0.1 µm filter-sterilized PBS (pH 7.0 – 7.2) and washed from blood by changing the PBS solution 3 times. Each organ sample was manually sliced in axial and sagittal planes in sterile tissue culture dish kept on ice. Individual tissue slices were then placed onto the uncoated 35 mm imaging dishes with No. 0 coverslip and 20 mm glass diameter (MatTek, #P35G-0-20-C). The slices were incubated in 500 µL FluoroBrightTM DMEM (TFS, #A1896701) supporting with 10% FBS, 1% PSA, and 4 mM L-Glutamine solutions. Mice (C57BL/6J, Jackson Laboratory) were used to obtain ex vivo skull samples, which were imaged directly without solution-based preparation.

Supporting Information

Supporting Information is available from the Wiley Online Library or from the author.

Acknowledgements

The authors thank Dianwen Zhang for helping with TIRF experiments. This work was supported by a grant from the National Institutes of Health (R01 CA241618).

[Correction added on 24 July 2024, after first online publication: references 9 and 10 have been updated in this version.]

Conflict of Interest

G.W. and H.T. are contacting the Office of Technology Management at the University of Illinois at Urbana-Champaign for commercial potential of the developed technology. Other authors declare no competing interests.

Author Contributions

G.W., R.R.I, and J.E.S. contributed equally to this work. G.W. and H.T. conceived the idea. H.T. and S.A.B. obtained the funding and supervised the study. R.R.I., J.E.S., J.S., and Y.S. developed parts of the methodology. R.R.I., J.E.S., and G.W. developed data acquisition software. G.W., J.E.S., R.R.I., E.A., C.A.R, E.J.C., and J.P. performed experiments. G.W., H.T., J.E.S., and R.R.I. performed data analysis. H.T. and G.W. drafted the manuscript. H.T. and S.A.B. reviewed and edited the manuscript with inputs from all authors.

Data Availability Statement

The data that support the findings of this study are available from the corresponding author upon reasonable request.

Keywords

fluorescence microscopy, multiphoton microscopy, POISSON photon statistics, quantitative microscopy

Received: January 5, 2024
Revised: June 14, 2024
Published online:

[1] J. C. Waters, *J. Cell Biol.* **2009**, *185*, 1135.
[2] P. Montero Llopis, R. A. Senft, T. J. Ross-Elliott, R. Stephansky, D. P. Keeley, P. Koshar, G. Marqués, Y.-S. Gao, B. R. Carlson, T. Pengo, M. A. Sanders, L. A. Cameron, M. S. Itano, *Nat. Methods* **2021**, *18*, 1463.
[3] O. Faklaris, L. Bancel-Vallée, A. Dauphin, B. Monterroso, P. Frère, D. Geny, T. Manoliu, S. de Rossi, F. P. Cordelières, D. Schapman, R. Nitschke, J. Cau, T. Guilbert, *J. Cell Biol.* **2022**, *221*, e202107093.
[4] M. Balu, A. Mazhar, C.-K. Hayakawa, R. Mittal, T.-B. Krasieva, K. König, V. Venugopalan, B. J. Tromberg, *Biophys. J.* **2013**, *104*, 258.
[5] S. R. Kantelhardt, D. Kalasauskas, K. König, E. Kim, M. Weinigel, A. Uchugonova, A. Giese, *J. Neuro-Oncol.* **2016**, *127*, 473.
[6] W. C. Lemon, K. McDole, *Curr. Opin. Cell Biol.* **2020**, *66*, 34.
[7] S. You, H. Tu, E. J. Chaney, Y. Sun, Y. Zhao, A. J. Bower, Y.-Z. Liu, M. Marjanovic, S. Sinha, Y. Pu, S. A. Boppart, *Nat. Commun.* **2018**, *9*, 2125.
[8] M. Žurauskas, M. Durack, H. Tu, S. A. Boppart in *Advanced Biomedical and Clinical Diagnostic and Surgical Guidance Systems XX*, SPIE, , **2022**, *11949*, 41.
[9] G. Wang, S. A. Boppart, H. Tu, *J. Biomed. Opt.* **2024**, *29*, 036501.
[10] G. Wang, J. Shi, R. R. Iyer, J. E. Sorrells, H. Tu, *arXiv preprint* arXiv:2305.08266, **2023**.

[11] R. Galli, O. Uckermann, E. F. Andresen, K. D. Geiger, E. Koch, G. Schackert, G. Steiner, M. Kirsch, *PLoS One* **2014**, *9*, e110295.
[12] K. König, P. So, W. Mantulin, E. Gratton, *Opt. Lett.* **1997**, *22*, 135.
[13] H. Tu, S. A. Boppart, *Laser Photonics Rev.* **2013**, *7*, 628.
[14] H. Tu, Y. Liu, D. Turchinovich, M. Marjanovic, J. K. Lyngsø, J. Lægsgaard, E. J. Chaney, Y. Zhao, S. You, W. L. Wilson, B. Xu, M. Dantus, S. A. Boppart, *Nat. Photonics* **2016**, *10*, 534.
[15] R. K. Benninger, W. J. Ashby, E. A. Ring, D. W. Piston, *Opt. Lett.* **2008**, *33*, 2895.
[16] L.-C. Cheng, N. G. Horton, K. Wang, S.-J. Chen, C. Xu, *Biomed. Opt. Express* **2014**, *5*, 3427.
[17] J. D. Driscoll, A. Y. Shih, S. Iyengar, J. J. Field, G. A. White, J. A. Squier, G. Cauwenberghs, D. Kleinfeld, *J. Neurophysiol.* **2011**, *105*, 3106.
[18] M. N. Modi, K. Daie, G. C. Turner, K. Podgorski, *Opt. Express* **2019**, *27*, 35830.
[19] V. D. Ching-Roa, E. M. Olson, S. F. Ibrahim, R. Torres, M. G. Giacomelli, *Sci. Rep.* **2021**, *11*, 5248.
[20] L. Li, M. Li, Z. Zhang, Z.-L. Huang, *J. Innov. Opt. Health Sci.* **2016**, *9*, 1630008.
[21] A. E. Lita, A. J. Miller, S. W. Nam, *Opt. Express* **2008**, *16*, 3032.
[22] J. Ma, S. Masoodian, D. A. Starkey, E. R. Fossum, *Optica* **2017**, *4*, 1474.
[23] J. E. Sorrells, R. R. Iyer, L. Yang, E. M. Martin, G. Wang, H. Tu, M. Marjanovic, S. A. Boppart, *ACS Photonics* **2022**, *9*, 2748.
[24] A. Lahlou, H. S. Tehrani, I. Coghill, Y. Shpinov, M. Mandal, M.-A. Plamont, I. Aujard, Y. Niu, L. Nedbal, D. Lazar, P. Mahou, W. Supatto, E. Beaurepaire, I. Eisenmann, N. Desprat, V. Croquette, R. Jeanneret, T. L. Saux, L. Jullien, *Nat. Methods* **2023**, *20*, 1930.
[25] N. G. Horton, K. Wang, D. Kobat, C. G. Clark, F. W. Wise, C. B. Schaffer, C. Xu, *Nat. Photonics* **2013**, *7*, 205.
[26] J. Zwier, G. Van Rooij, J. Hofstraat, G. Brakenhoff, *J. Microsc.* **2004**, *216*, 15.
[27] C. M. Brown, A. Reilly, R. W. Cole, *J. Biomol. Tech.* **2015**, *26*, 37.
[28] C. M. Hobson, M. Guo, H. D. Vishwasrao, Y. Wu, H. Shroff, T.-L. Chew, *Nat. Methods* **2022**, *19*, 1538.
[29] X. Chen, U. Leischner, Z. Varga, H. Jia, D. Deca, N. L. Rochefort, A. Konnerth, *Nat. Protoc.* **2012**, *7*, 1818.
[30] O. I. Kolenc, K. P. Quinn, *Antioxidants and Redox Signaling, ars* **2017**, *7451*, 2017.
[31] J. M. Murray, P. L. Appleton, J. R. Swedlow, J. C. Waters, *J. Microsc.* **2007**, *228*, 390.
[32] K. W. Dunn, R. M. Sandoval, K. J. Kelly, P. C. Dagher, B. A. Molitoris, *Am. J. Physiol. Cell Physiol.* **2002**, *283*, C905.
[33] W. Zheng, D. Li, Y. Zeng, Y. Luo, J. Y. Qu, *Biomed. Opt. Express* **2011**, *2*, 71.
[34] M. Ning, M. A. Digman, L. Malacrida, E. Gratton, *Biomed. Opt. Express* **2016**, *7*, 2441.
[35] M. Wahl, T. Röhlicke, S. Kulisch, S. Rohilla, B. Krämer, A. C. Hocke, *Rev. Sci. Instrum.* **2020**, *91*, 013108.
[36] Y. Rivenson, H. Wang, Z. Wei, K. de Haan, Y. Zhang, Y. Wu, H. Günaydin, J. E. Zuckerman, T. Chong, A. E. Sisk, L. M. Westbrook, W. D. Wallace, A. Ozcan, *Nat. Biomed. Eng.* **2019**, *3*, 466.